

# Investigation of NGC 2323

Group 1: Finn Beckingsale, Jedd Thomas and Petros Koutroumpinas



Figure 1: Image of NGC 2323 taken with the Takahashi Epsilon 180 Hyperbolic astrograph telescope (Espenak 2022).

## Abstract

In this report, we investigate the properties of the open cluster NGC 2323 using images taken using the Hutton-Westfold Observatory (C14). By converting photon counts to an apparent magnitude and then absolute magnitude using age-luminosity isochrones, we calculated the distance to the open cluster, allowing us to use the mass relation to calculate the initial mass function of the cluster. We determined the age of the cluster to be  $150 \text{ Myr} \pm 10 \text{ Myr}$  and the distance to be  $954 \text{ pc} \pm 40 \text{ pc}$ . The age value corresponds nicely with the literature value of  $140 \text{ Myr}$  (Frolov, Ananjevskaja and Polyakov 2012). There was a larger difference when it came to the distance calculation, which had a literature value of  $902 \text{ pc}$  (Dib, Schmeja & Parker 2018).

## 1. Introduction

The ‘heart shaped’ open cluster NGC 2323, also known as Messier 50, exists on the edge of the CMA OB1 nebula from which it is believed to have originated (Clarià et al. 1997). Open clusters are groups of stars that were formed in the same stellar nursery and are loosely gravitationally held together. Due to this low gravitational attraction and similar origin, open clusters harbour stars which are young -under a billion years old- and have similar metallic compositions (Payne-Gaposchkin 1979), making them useful for capturing historical information about specific periods in the universe. Additionally,

open clusters are important for studying stellar evolution as they represent a vast number of stars at the same age.

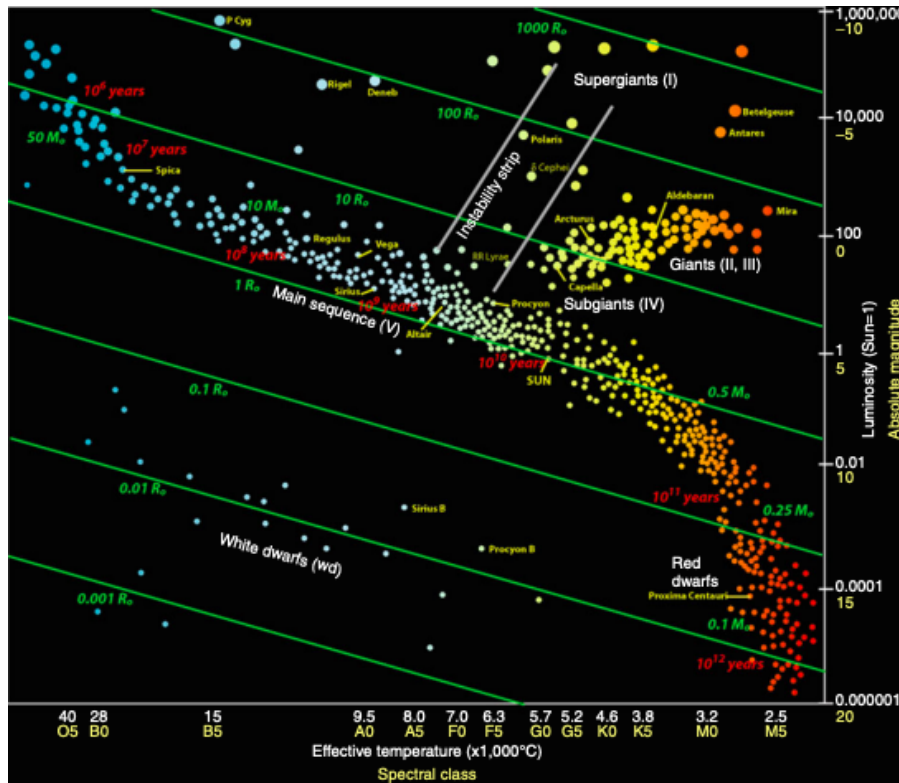


Figure 1.1: Hertzsprung-Russell diagram labelled with respective star types for different regions (Gargaud 2011).

The Hertzsprung-Russell (HR) diagram depicts the evolution of stars, as it shows the surface temperature and respective magnitude for stars, which can be then utilised to estimate the evolution of clusters. Using isochrones, which represent a HR diagram for specific stellar ages, the turnoff from the main sequence and toward the giant branch (Figure 1.1) can be compared with raw stellar data in order to find the age of a cluster, since all the stars in the cluster have approximately the same age. Once the most fitting isochrone and corresponding age are found, the difference in absolute magnitude approximated by the isochrone can be compared to the apparent magnitude of the stellar data to find a distance modulus, which is then used to find the distance of the cluster using Equation (1.1).

$$(1.1) \quad d = 10 * 10^{\frac{m-M}{5}}$$

Where  $d$  is the distance in parsecs,  $m$  is the apparent magnitude and  $M$  is the absolute magnitude.

Another important use of open clusters is in studying stellar formation, as the stellar masses of clusters can be used to create an initial mass function (IMF), usually represented in a form similar to Equation (1.2). The IMF can be used to further understand the initial star forming conditions of clusters, which vary in level of ambient temperature, metallicity and density (Lim et al. 2015).

$$(1.2) \quad \xi(m) \propto m^{-\alpha}$$

Where  $\xi$  is the stellar number density as a function of mass,  $m$  is the mass and  $\alpha$  is the exponent relating stellar density to mass.

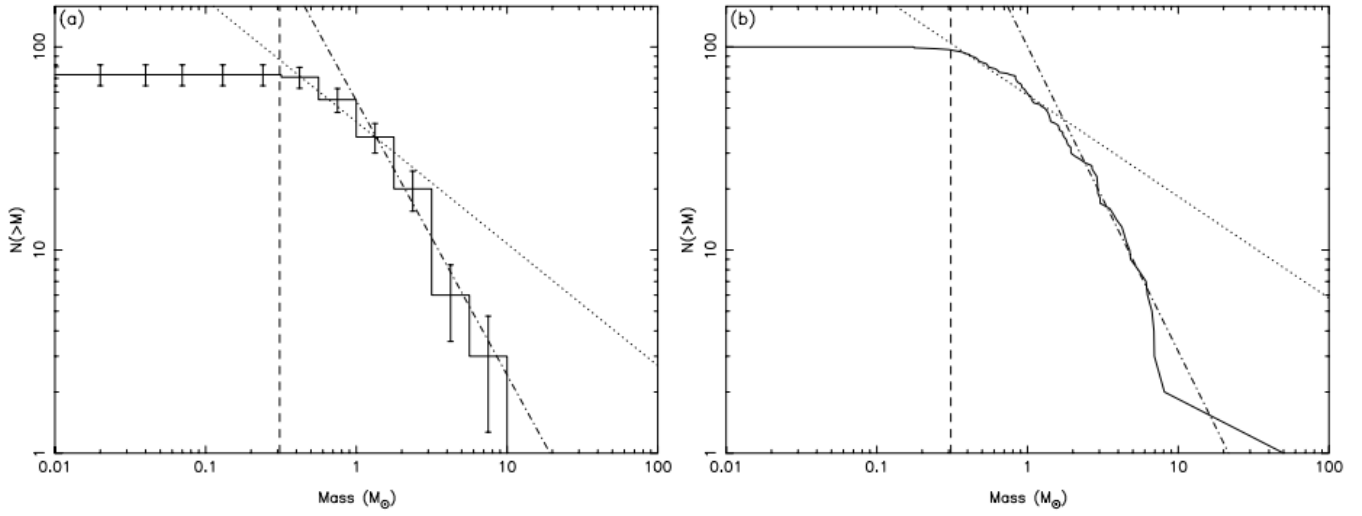


Figure 1.2: Initial mass distribution for the BN finger of the Orion constellation, showing the data (left) and the polynomial fit on the right (Lim et al. 2015).

We can see from Figure 1.2 that within stellar formation there are generally more lower mass stars in clusters, and the numbers drop off at very large masses relative to the Sun's mass. This is the distribution expected for the NGC 2323 open cluster.

## 2. Methodology

Observations of NGC 2323 were captured on March 23rd, 2022 using the C14 telescope at the Hutton-Westfold Observatory, with cloud cover varying throughout the observation. Due to the varying cloud cover, the flat images were captured on April 1st, 2022 by Michael Brown. The first exposures were captured with a one-second exposure time, which produced our bias images. The next exposures were the light images and were captured using the B, V, and R-Band filters. Ten 10-second exposures were captured initially using the respective bands to ensure the telescope had been focused and was tracking correctly. Five 120-second exposures were then captured using the B and V-Band after their respective checks. Due to the cloud cover increasing towards the end of the observations, only ten 60-second exposures were captured using the R-band filter due to the tracking no longer working. Finally, the CCD was left running overnight to capture seven 3600-second dark exposures.

$$\begin{aligned}
 light' &= light - bias' \\
 dark' &= dark - bias' \\
 flat' &= flats - bias \\
 light'' &= light' - \alpha dark' \\
 flat'' &= flat' - \beta dark' \\
 proc\ images &= light'' / flat''
 \end{aligned}$$

Equation (2.1): Procedure for processing images capture, where  $\alpha$  and  $\beta$  are exposure time scaling factors (Rieke 2012).

### *Reducing Images*

Using Jupyter Notebook and Python, Equation (2.1) was followed to produce our processed images. First the bias images were combined into a single image using a median combine, which is denoted by *bias'* in Equation (2.1). The *bias'* image was then subtracted from the light images to remove hot pixels and random fluctuations, which is denoted as *light'*. The dark and flat images were then median combined and had *bias'* subtracted from the single image to produce *dark'* and *flat'* respectively. The *light'* and *flat'* images then had the *dark'* image scaled to the respective exposure time and subtracted, creating *light''* and *flat''*. The final processed images are then produced by dividing *light''* by *flat''*.

### *Shifting and Scaling*

Using DS9 to visually inspect the processed images, a common star was chosen to be used as the centroid, and using python, the pixel coordinates of the centroid were found for the B, V, and R-band images using a 2D gaussian fit. Next, each band's images were shifted by aligning the centroid to the same pixel coordinates in each image. Once each band's images had been shifted, the images were then scaled and combined to create two separate images, a median combined image, and a mean combined image. The median combined images (Figure 2.1) were created from each pixel's average value across the images being combined, whereas the mean combines (Figure 2.2) were created from the pixel's mean values. After visually inspecting our combines using DS9, it was determined that the median fit was the clearest of the two combines.

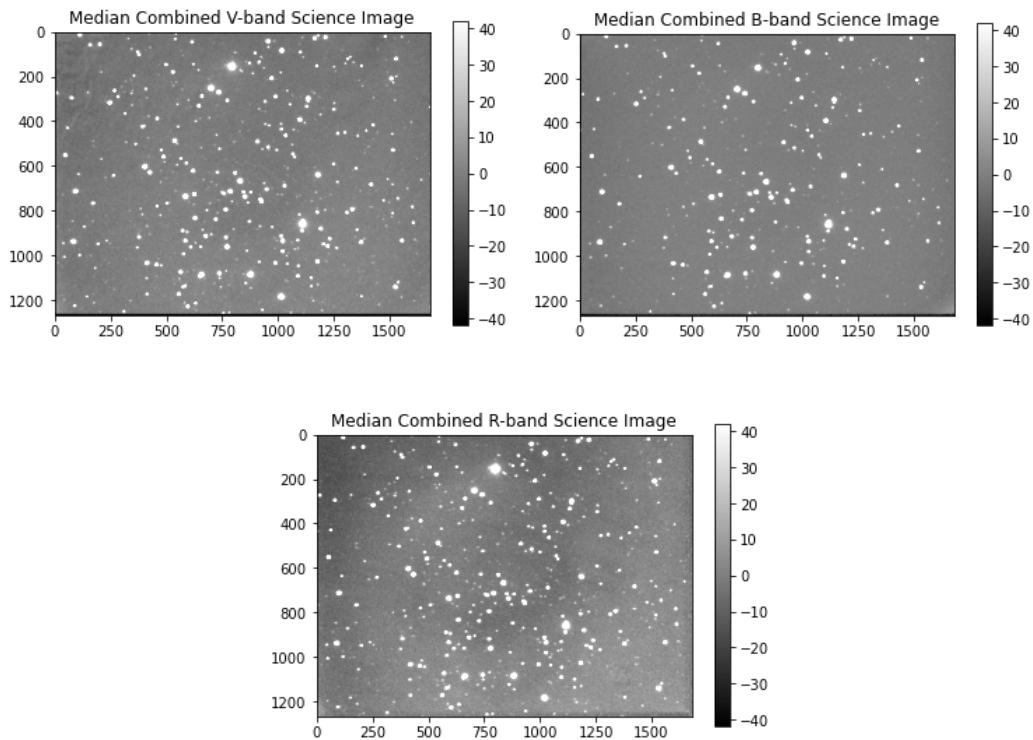


Figure 2.1: Median combined V-band, B-band and R-band science images of NGC 2323



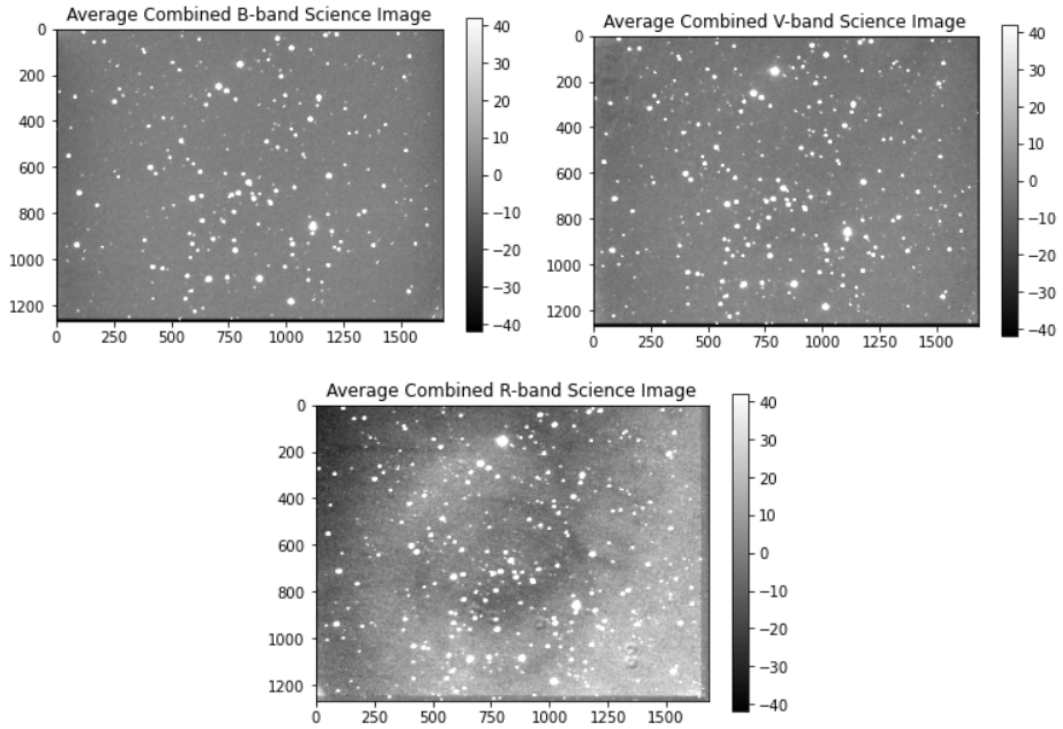


Figure 2.2: Average combined V-band, B-band and R-band science images of NGC 2323

### *Photometry*

Each median image was then run through code, which found stars by locating peak ADU counts in the given image. The location data was then printed over their respective images and it was determined that the R-band gave the most accurate positions for stars (Figure 2.3).

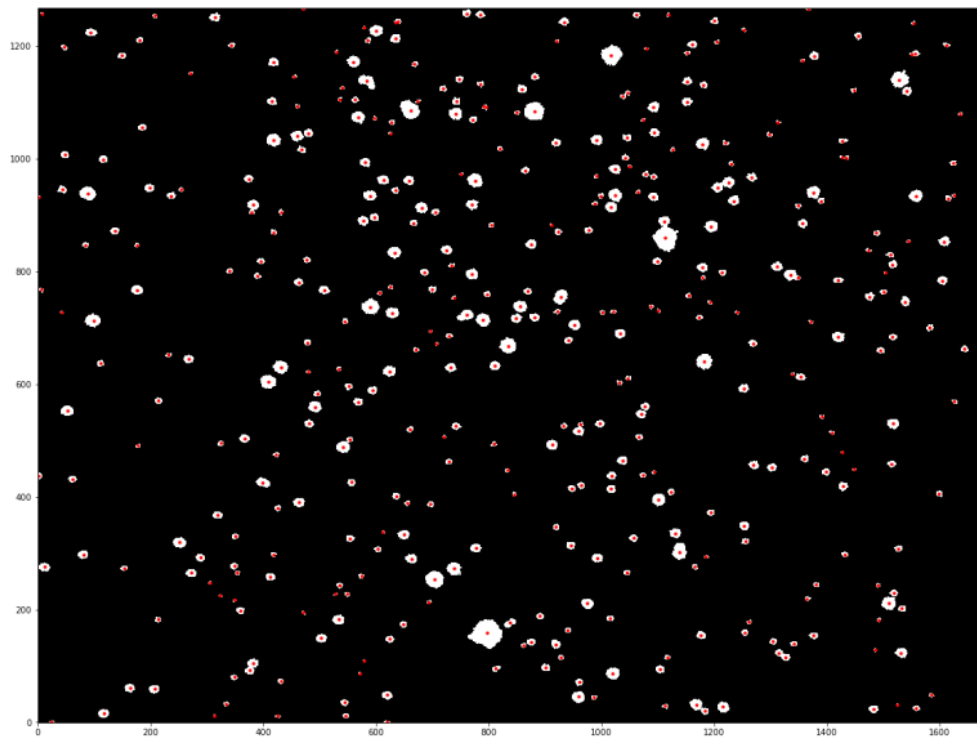


Figure 2.3: Median Combined R-Band of NGC 2323 overlaid with star locations found by analysis.

As the combines were shifted using the same star, the locations found in Figure 2.3 were able to be applied to the B-Band and V-Band images with some minor shifts in both axes.

Using AladinLite, a reference star was chosen to calibrate our ADU to magnitude calculations. Finally using Equation (2.2), the apparent magnitude of each star was determined.

$$(2.2) \quad m_v = -2.5 \log_{10}(ADU/ADU_0) + M_{v,0}$$

$$m_b = -2.5 \log_{10}(ADU/ADU_0) + M_{b,0}$$

Where  $v$  is V-band,  $b$  is B-band,  $m$  is apparent magnitude,  $M$  is absolute magnitude and variables subscripted with 0 are the reference star.

### 3. Results and Discussion

What can be seen in both the median and average combined images in figures 2.2 and 2.3, is that there were issues with the R band images. These were caused by cloud interference, due to this their photometry values were not used.

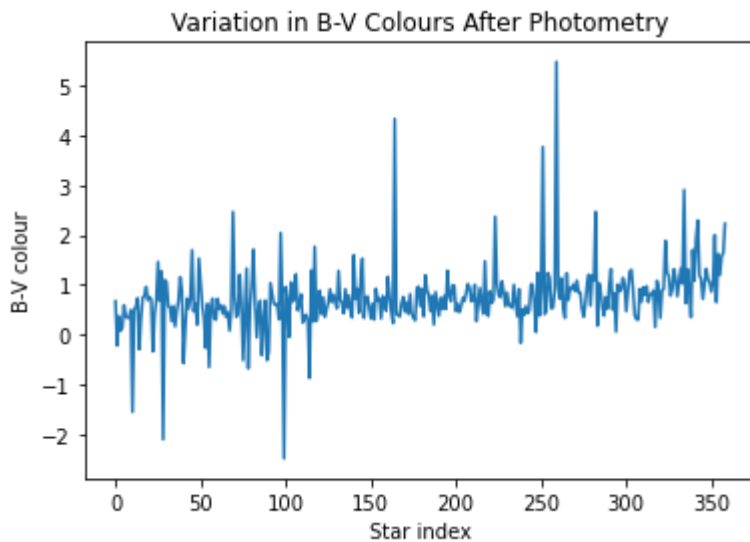


Figure 3.1: Plot of the catalogue of 359 stars and each of their indexes and corresponding colours.

Figure 3.1 shows the colours for each of the objects following our photometry. We see a relatively consistent B-V colour for our objects, which agrees with what would be expected for an open cluster of stars with similar age. The colours occur in the range between approximately -0.5 and 2, with outliers, which corresponds to the colours expected from O5 type stars (-0.33) and M7 type stars (1.80) (Carroll and Ostlie 2017). This means we have a good range of different star types with which to fit isochrones.

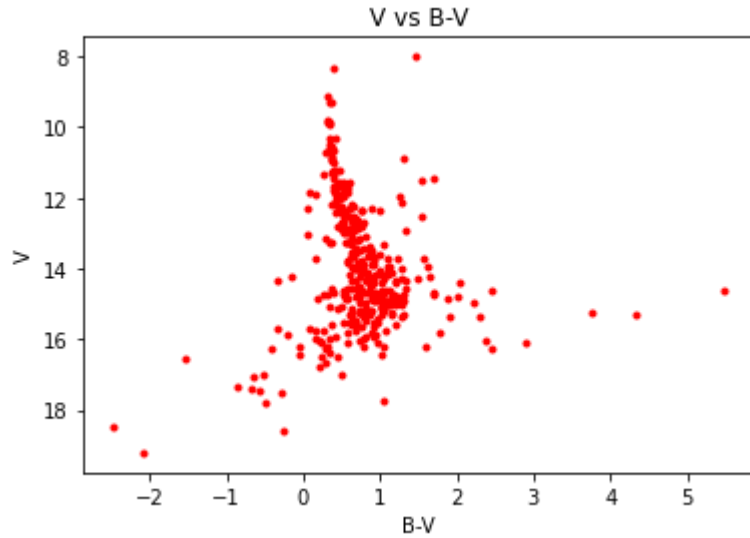


Figure 3.2: Plot of V-band apparent magnitude versus B-V colour for 359 stars.

Following the plot of magnitude versus colour in Figure 3.2, we can see that there is a noticeable downward trend, which agrees with the Hertzsprung-Russell diagram (Figure 1.1). There are also some visible outliers, which are likely due to objects being cut off at the perimeters of either our B or V-band science images following shifting. For the purposes of fitting the isochrone, we focused on the central congregation of stellar objects.

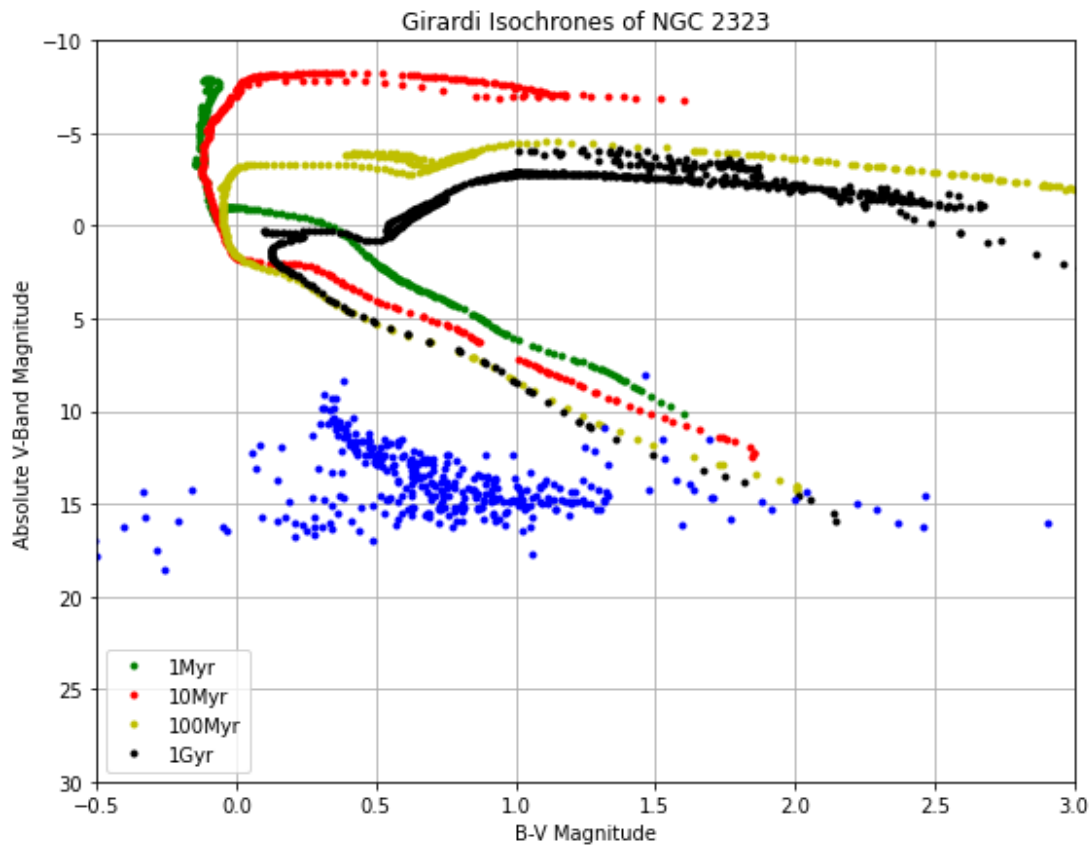


Figure 3.3: Girardi isochrones plotted over stellar data (blue) for 1Myr, 10Myr, 100Myr and 1Gyr.

The Girardi isochrones have similar trends on the main sequence (between magnitudes 5 and 15 and B-V colours 0.5 and 2), but differ in their point of turn-off from the main-sequence (Figure 3.3). From Figure 3.3 there is a visible turn-off in the NGC 2323 data at a B-V colour of 0.4. The only age which fits the curvature of the turnoff is 100 Myr, as 1 Myr and 10 Myr isochrones curve off too slowly and the 1 Gigayear isochrone turns off too rapidly. To shift the data to fit the 100 Myr isochrone, we added a redshift of 0.4 in colour, then adjusted the absolute V-band magnitude of the data to get a distance modulus.

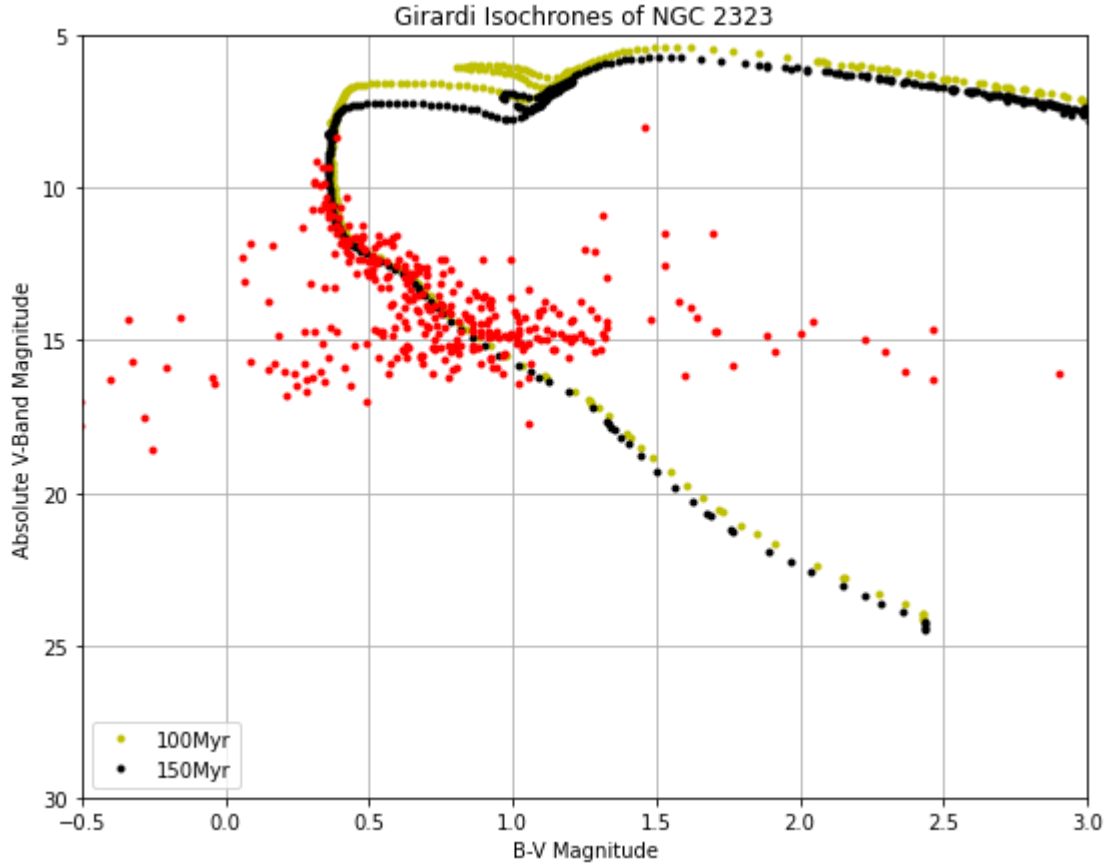


Figure 3.4: Redshift and distance adjusted NGC 2323 data over 100Myr and 150Myr isochrones.

After adjusting the V-band magnitude by 9.9 and the colour by 4.1, the most fitting isochrones were found to be for ages of 100 and 150 Myr (Figure 3.4), so we estimated the age of NGC 2323 to be  $125 \pm 25$  Myr. This result agrees with academic results of 130 Myr (Kalirai et al. 2003). Due to the isochrones being in absolute magnitudes, the V-band magnitude adjustment can be used as a distance modulus, and we can determine the distance of NGC 2323 based on Equation (3.1).

$$(3.1) \quad d = 10 * 10^{\frac{9.9}{5}} = 950 \pm 150 \text{ parsecs}$$

The result in Equation (3.1) calculating a distance from NGC 2323 of  $950 \pm 150$  parsecs agrees with parallax estimates of  $1000 \pm 140$  parsecs (Oralhan 2021). The uncertainty was based on the likely human error in fitting the isochrone to the trend of NGC 2323 stellar data.



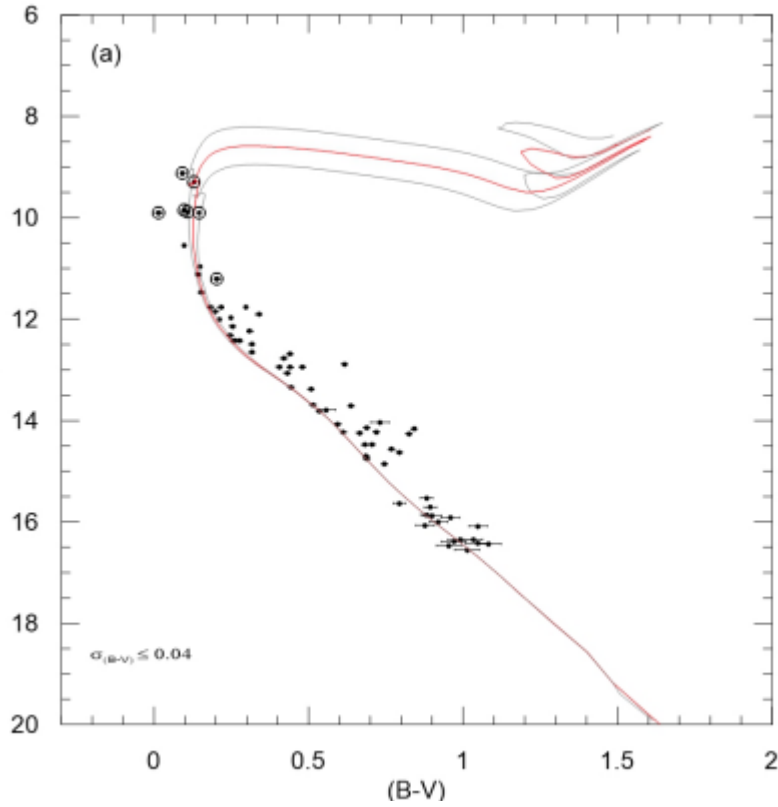


Figure 3.5: 150 Myr, 200 Myr, and 250 Myr isochrones for metallicity  $Z=0.012$  plotted over data for NGC 2323 (Oralhan et al. 2019).

When comparing our fitted isochrone (Figure 3.4) to that found by Oralhan et al. (2019) (Figure 3.5), we see that their adjustment for a metallicity of 0.012 instead of our assumed solar metallicity of 0.02 results in a higher estimate of the cluster's age. The data is in the same range as our own, with most V-band magnitudes being within 10-18, and B-V colour being within the range 0-1.5. However, the resulting distance from the calculations still agrees with Oralhan et al. (2019) at  $1000 \pm 140$  Myr.

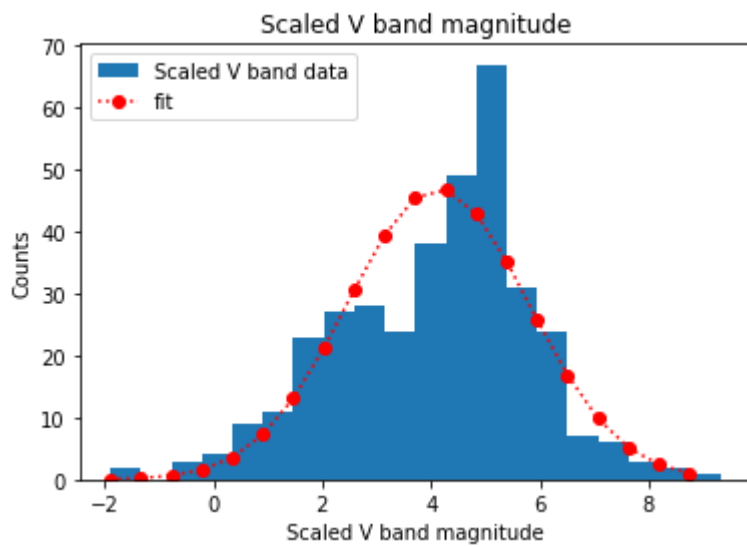


Figure 3.6: Histogram of the distribution of counts for V-band absolute magnitudes with bin length of 0.6, including a fitted Gaussian distribution (red).

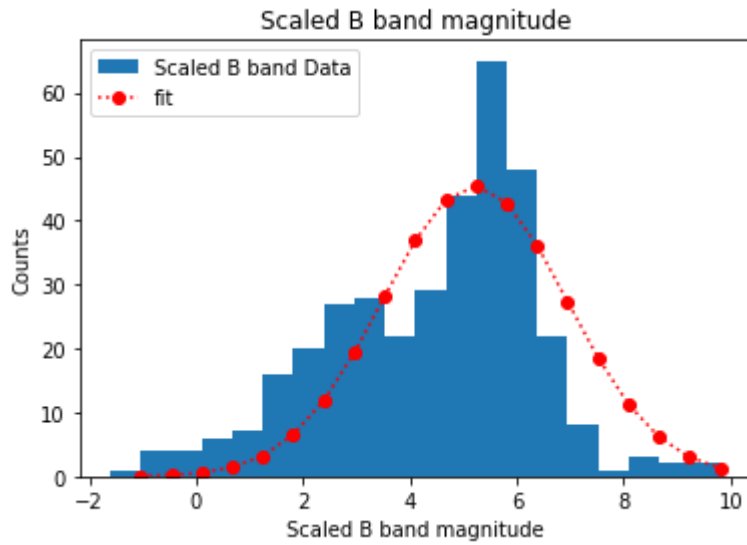


Figure 3.7: Histogram of the distribution of counts for B-band absolute magnitudes with bin length of 0.6, including a fitted Gaussian distribution (red).

The spread of counts in both the V and B-bands in Figures 3.6 and 3.7 is slightly skewed to the right due to higher magnitudes corresponding to lower mass. The Gaussian fits show a slight skewing to the right, however, the distributions are not as skewed as what would be expected from comparing to Figure 1.2. This is likely due to a lack of detectability for stars dimmer than 7 magnitudes, and is why the counts drop off so steeply.

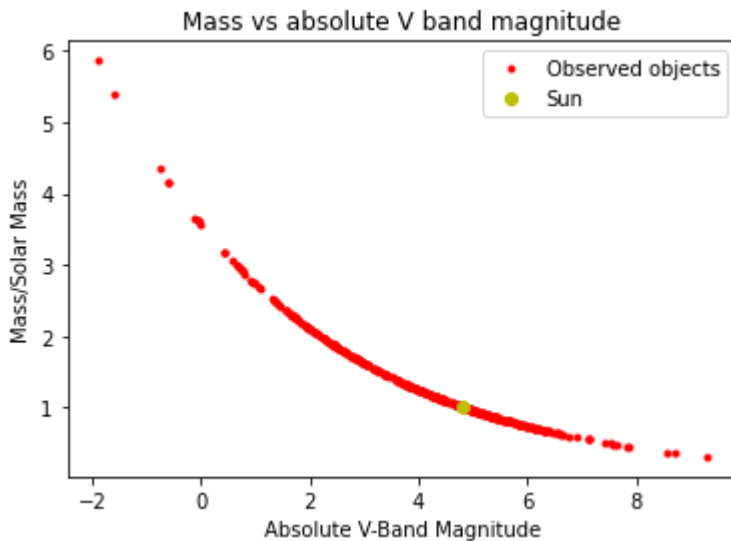


Figure 3.8: Relation between the Mass of a star per solar mass versus its absolute V-band magnitude, with statistics of the Sun included for comparison (Williams 2018).

As expected, when the mass of the star drops the magnitude of the star increases (Figure 3.8), meaning that the star is fainter. Adding the statistics for the Sun to this plot shows that our relation is in agreement with the Sun.

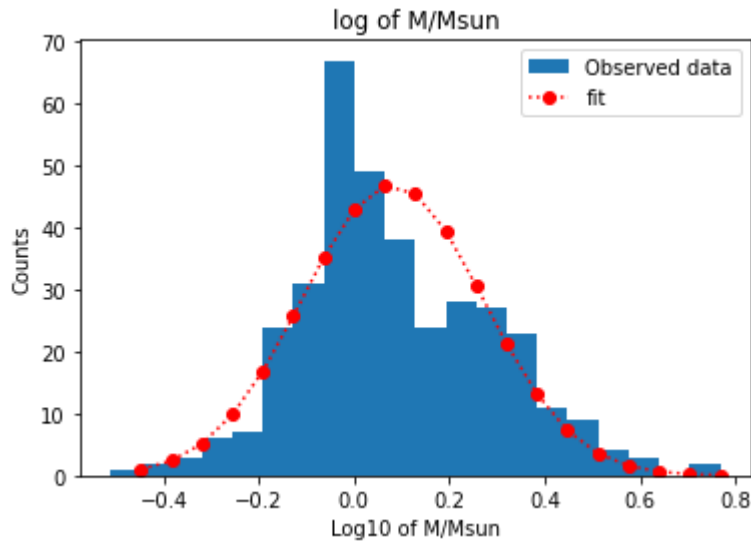


Figure 3.9: Histogram showing logs of the ratios of the mass of the stars to solar mass, with bin length of 0.06.

For the initial mass function, a few changes were made to the data. First, everything under 0 (or 1 solar mass) was ignored. This was due to objects smaller than the sun being difficult to observe, which leads to there being far fewer objects below 0 when there should be more of them (Figure 3.9), leading to an incorrect initial mass function. The last two data points were also ignored, as the second last data point was a zero and returned an error when taking its log.

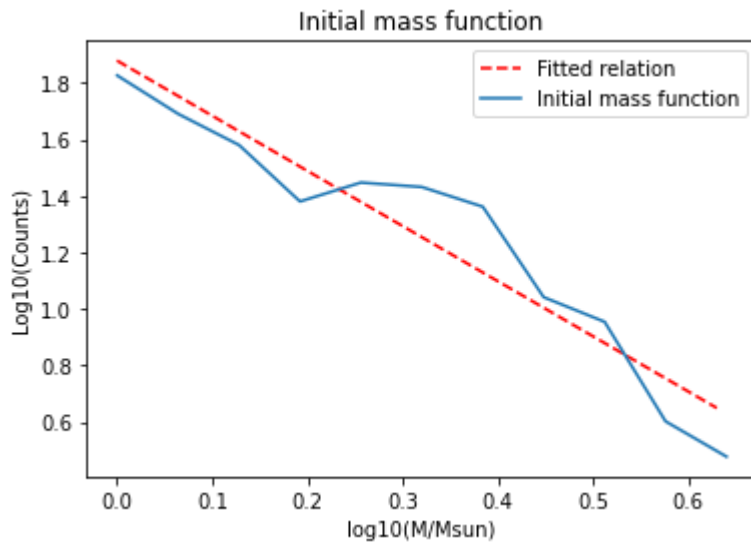


Figure 3.10: log-log plot of stellar counts vs mass of NGC 2323, with a fitted linear relation.

With the log plot of the data in Figure 3.9 we were able to fit a linear relation between the counts and masses. This gave us the following relation:

$$(3.2) \quad \log(count) = -1.95\log(mass) + 1.8$$

Following the relation in Equation (3.2) we were able to find the  $\alpha$  index (Equation (1.2)) to be  $2.0 \pm 0.3$ , in accordance with the coefficient for the log-log relation. This is outside one standard deviation of the index for Salpeter Function for initial mass, which is 2.35 (Salpeter 1955). This variation is likely due to different initial stellar formation conditions compared to the average calculated by Salpeter.

## 4. Limitations

Due to limitations on brightness for detection, some of the stars in the NGC 2323 cluster were not able to be catalogued. Our final list of stellar objects had 359 entries after selecting for only the objects visible in both the V and B-band images, whereas the expected number of stars in NGC 2323 is 497 (Armin et al. 2017). Likely all 138 of these stars were under 1 solar mass, or above 5 in absolute magnitude, since this is where the counts begin to drop off. There is another potential factor reducing the number of catalogued stars which will be explored in Section 5. To improve count results, we would need a much more powerful telescope or satellite that could resolve and locate the last 80 low mass stars in NGC 2323.

Apart from stars that were not catalogued due to faint magnitudes, there are also likely to be foreground and background stars within the data, not from NGC 2323, that have not been accounted for. This likely explains the spread of values in Figure 3.4.

Additionally, we were unable to adjust the absolute magnitude for dust reddening, which is an important factor which makes objects appear dimmer and therefore further away. Next time, research should be conducted to find the approximate dust reddening affecting the magnitude in both the V and the B-bands.

## 5. Extension

### 5.1 Initial Mass Function Implications

IMFs are important for analysing and following the initial conditions of regions in galaxies. Velocity dispersion and metallicity determine the initial mass function, with approximately 50% of  $\alpha$  variation explained by metallicity (Villaume et al. 2017). The more metallic, the higher the skewing towards high counts at low masses. Metallicity is dependent on star age and rate of star formation, and also is inversely proportional to galactocentric distance (Plotner 2017).

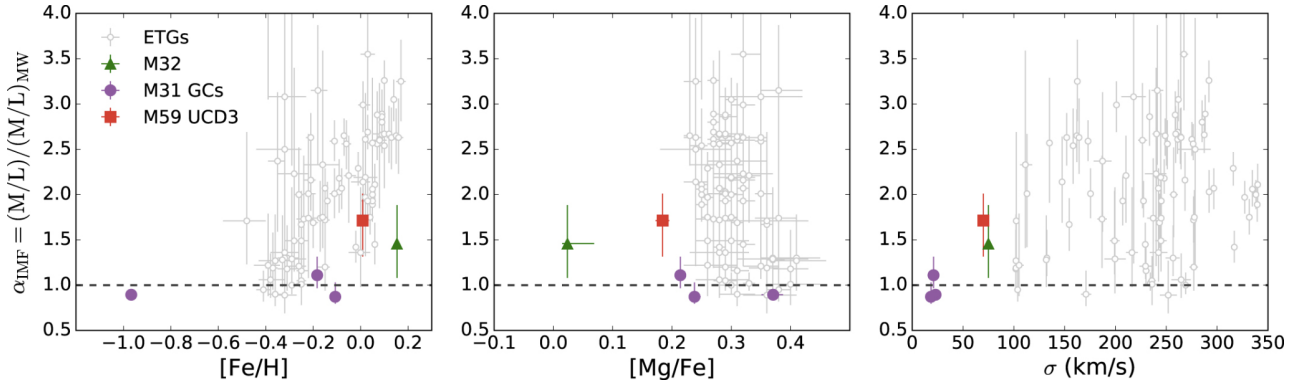


Figure 5.1.1:  $\alpha$  index of clusters in the Milky Way versus iron content, magnesium content and velocity dispersion (Villaume et al. 2017)

From the data in Figure 5.1.1, which catalogues the calculated  $\alpha$  for various clusters within the Milky Way, we see in the first image an upward trend implying a positive relation between iron content and  $\alpha$  index for the relation in Equation 1.2. Looking at the data, and with NGC 2323 having an  $\alpha$  index of  $2.0 \pm 0.3$ , we estimate an iron content ( $\text{Fe}/\text{H}$ ) of  $-0.2 \pm 0.2$  for NGC 2323. The reason such a broad statement about a cluster of many stars can be made is due to all the stars being formed at similar times in the same region, giving similar metallicities. According to an  $\text{Fe}/\text{H}$  of  $-0.2$ , the cluster has a metallicity 0.6 times that of the Sun. Previous research has found a metallicity for NGC 2323 of  $0.012 \pm 0.003$  (Oralhan et al. 2019), corresponding to an iron content of  $-0.22 \pm 0.01$ , which agrees within a standard deviation of our estimate. A low metallicity implies either that the stars are old or that this region has a low rate of star formation. We already found the age to be  $125 \pm 25$  Myr, which is much younger than the Sun's age of  $\sim 4.6$  Gyr. Therefore, NGC 2323 must exist in a region of slow star formation.

The relation of  $\alpha$  to velocity dispersion on the far right graph in Figure 5.1.1 is less obvious. Due to the lack of an obvious trend, velocity dispersion for NGC 2323 at an  $\alpha$  of 2.0 was approximated to be  $200 \pm 150$  km/s. However, This result is quite inaccurate and does not give us much more information.

## 5.2 Initial - final mass function of White dwarfs

The initial - final mass relation is the connection between the masses of white dwarfs and the mass that they had when they were main sequence stars (Cataln, Isern, Garca-Berro and Ribas, 2008). Up until now, astronomers have not been able to measure this relation accurately. A survey in 2016 of the white dwarf stars in NGC 2323 (Cummings et al 2016) attempted to further investigate this relation using 10 potential white dwarf stars. Six of the white dwarfs were eliminated from the catalogue of 10 due to a high signal-to-noise ratio. The loss of these stars had to be supplemented by using publicly available white dwarf star data.

An observation such as the one that was carried out in this report could be used to clear up the signal-to-noise issue with the six stars and make them usable in future surveys. Knowing the initial - final mass relation would mean that we know how the open cluster will evolve in future and what remnants would be left once most of the stars have left the main sequence.

### 5.3 Cluster ages

The normal age of an open cluster is expected to be from millions of years to 1 Gyr (earthsky.org, 2020). An analysis was carried out using 800 Myr as the age where open cluster extinction is suspected to occur and using data from Astrophysical parameters of Galactic open clusters (Kharchenko et al, 2005) to compare the cluster and star evolution trends.

Using  $t \propto M^{-2.5}$  the life expectancy of all the stars was calculated.

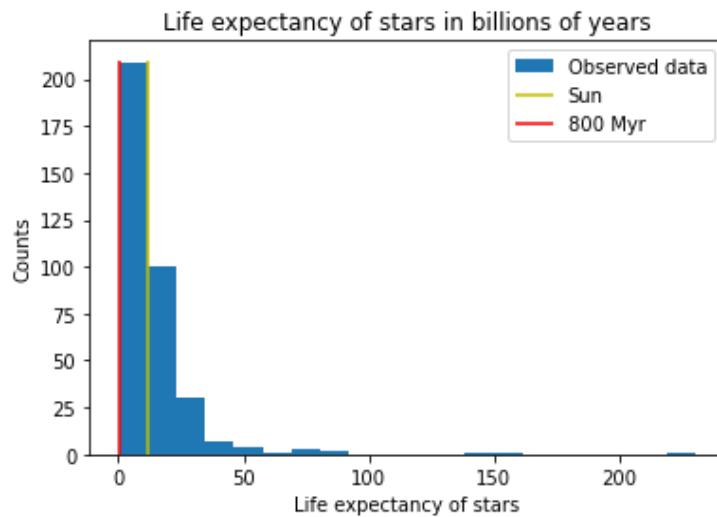


Figure 5.3.1: Life expectancy of stars in the NGC 2323 compared with the sun.

It is expected that 96.1% of stars (345 out of 359) will live beyond 800 Myr. This was antithetical to what the Kharchenko et al. catalogue showed which was that by this point most of the open clusters will have dissipated (shown in the figure below)

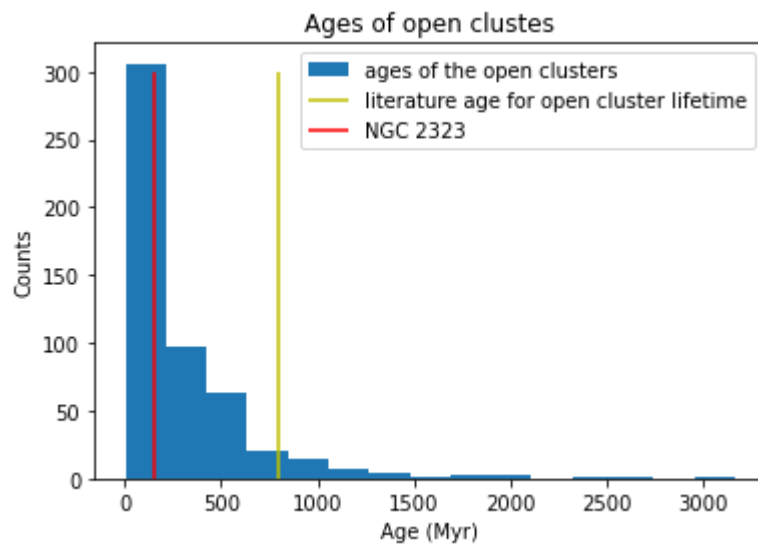


Figure 5.3.2: Ages of the open clusters with the red line being the age of NGC 2323 and the yellow line being the expected maximum age of open clusters.



Figure 5.3.2 shows that by the time 4% of the stars have died within NGC 2323 it is expected that 93% of the open clusters will have fallen apart. An occurrence that could be skewing these results is the fact that large bright stars tend to die out on a similar timescale to the life of the open clusters. The lack of the brightest objects in the cluster would make it more difficult to observe.

## 5.4 Cluster dispersion

Using the Kharchenko et al. catalogue, the sizes of the open clusters are shown in the figure below.

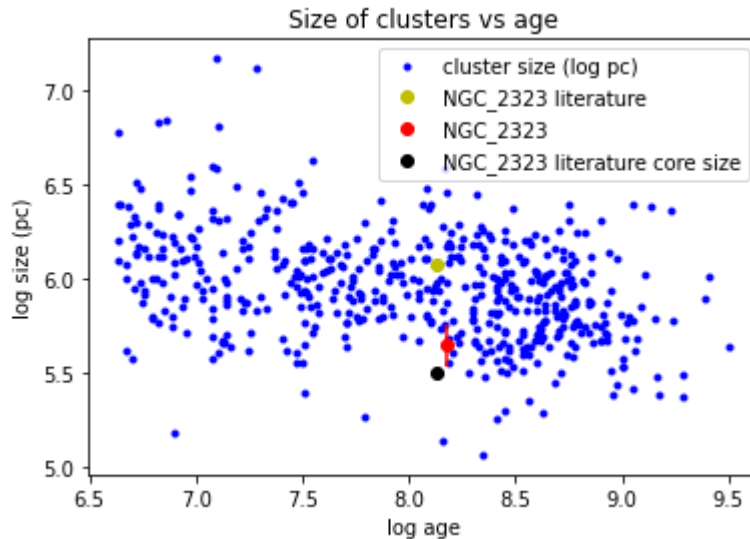


Figure 5.4.1: Sizes of open clusters as they increase in age.

What can be seen in Figure 5.4.1 is that as the open clusters get older they shrink in size. This could be due to the selection bias of the older open clusters having originally been very tightly bound clusters to begin with and the less tightly bound cluster having already fallen apart. The red dot represents the observed size for NGC 2323. The yellow dot and black dots are the catalogue values for NGC 2323 cluster size and core size respectively. This suggests that we are only observing the core of NGC 2323 instead of the entire cluster.

This would affect the solution that was found for the initial mass function as due to the effects of multi-body rotation the smaller stars would be ejected from the core into the ring of the open cluster. If these stars could have been observed this would have affected the results in figure 3.10 by making the gradient more negative bringing the results closer to the expected literature value of -2.3.

## 6. Conclusion

Following photometry of NGC 2323 in V, B and R band images, we were able to fit isochrones to estimate an age of  $125 \pm 25$  Myr, which agrees with previous estimates of 130 Myr (Kalirai et al. 2003) when assuming solar metallicity. However, when adjusting isochrones for metallicities of  $Z = 0.012$ , Oralhan et al. (2019) calculated an age of  $200 \pm 50$  Myr. The distance modulus taken from adjusting the isochrones gave us a distance to NGC 2323 of  $950 \pm 150$  parsecs, which agrees with previous calculations of  $1000 \pm 140$  parsecs (Oralhan et al 2019). After finding an initial mass function with an  $\alpha$  index of  $2.0 \pm 0.3$  and estimating an iron content (Fe/H) of  $-0.2 \pm 0.2$ , it is likely

that the metallicity of NGC 2323 is not similar to the Sun. To improve our age estimates in following studies, we should use isochrones with metallicities adjusted to an iron content of -0.2, instead of assuming solar metallicities. We saw that the age of NGC 2323 was normal when compared to the ages of the other open clusters but the size of the cluster was potentially on the smaller scale when compared to other studied open clusters.

## References

- Amin, M. and Elsanhoury, W. 2017. Astrometric and photometric study of the open cluster NGC 2323. *Serbian Astronomical Journal*, 59-69.
- Carroll, B., and Ostlie, D. 2017. *An Introduction to Modern Astrophysics* (2nd ed.). Cambridge: Cambridge University Press.
- Cataln, S., Isern, J., Garca-Berro, E. and Ribas, I., 2008. The initial final mass relationship of white dwarfs revisited: effect on the luminosity function and mass distribution. *Monthly Notices of the Royal Astronomical Society*, 387(4), pp.1693-1706.
- Clariá, J. J., Piatti, A. E. and Lapasset, E., 1997 'NGC2323: A Moderately Young Open Cluster in the Region of the Stellar Association CMaOB1'. *Boletín de la Asociación Argentina de Astronomía La Plata Argentina* 41, p. 73.
- Cummings J. D., Kalirai J. S., Tremblay P. E., Ramirez-Ruiz E. Two Massive White Dwarfs From NGC 2323 and the Initial-Final mass Relation from Progenitors of  $4 - 6.5 M_{\odot}$ , *The Astrophysical Journal*, 818:84 (13pp), 2016 February 10
- Dib, S., Schmeja, S. & Parker, Richard J., 2018. Structure and mass segregation in Galactic stellar clusters. *Monthly notices of the Royal Astronomical Society*, 473(1), pp.849–859.
- EarthSky | Updates on your cosmos and world. 2022. *What are 'open' star clusters?* | *Astronomy Essentials* | *EarthSky*. [online] Available at: <<https://earthsky.org/astronomy-essentials/definition-examples-what-are-open-star-clusters/>> [Accessed 28 May 2022].
- Espenak, F., 2022. *Messier 50 - M50*. [online] Astropixels.com. Available at: <<http://astropixels.com/openclusters/M50-01.html>> [Accessed 17 May 2022].
- Frolov, V., Ananjevskaja, Y. and Polyakov, E., 2012. 'Investigation of the open star cluster NGC 2323 (M50) based on the proper motions and photometry of its constituent stars'. *Astronomy Letters*, 38(2), pp.74-86.
- Gargaud, M. 2011. 'Hertzsprung Russell Diagram' [image]. *Encyclopaedia of Astrobiology*, Springer-Verlag Berlin Heidelberg.

Kalirai, J. S., Fahlman, G. G., Richer, H. B., and Ventura, P. 2003, 'The CFHT Open Star Cluster Survey. IV. Two Rich, Young Open Star Clusters: NGC 2168 (M35) and NGC 2323 (M50)', *The Astronomical Journal*, 126(3), pp. 1402–1414.

Kharchenko, N. V., et al., 2005. Astrophysical parameters of Galactic open clusters. *Astronomy and astrophysics (Berlin)*, 438(3), pp.1163–1173.

Lim, B., Sun H., Hur H. and Park B. G., 2015. The Initial Mass Function of Young Open Clusters in the Galaxy: A Preliminary Result, *International Astronomical Union*, (316), pp. 1-2.

Messier Objects. 2022. *Messier 50: Heart-Shaped Cluster - Messier Objects*. [online] Available at: <<https://www.messier-objects.com/messier-50-heart-shaped-cluster/>> [Accessed 17 May 2022].

Oralhan, İ.A., Michel, R., Schuster, W.J. et al. 2019. 'CCD UBV(RI)KC photometry of NGC 2323 and NGC 2539 open clusters', *J Astrophys Astron* 40(33), pp. 1-18.

Oralhan, İ. A., Karşlı, Y., Karataş, Y., Çakmak, H., Sung, H., and Michel, R. 2021, 'CCD UBV(RI)KC and GAIA photometry of NGC 2323, NGC 2539, Juchert 9 and Berkeley 97 open clusters', *COSPAR Scientific Assembly*, 43, p. 1539, 2021.

Payne-Gaposchkin, C. 1979. 'Stars and clusters'. *Cambridge: Harvard University Press*.

Plotner, T. 2017. 'Messier 50 – the NGC 2323 Open Star Cluster', *Universe Today*, viewed 23 May 2022. <https://www.universetoday.com/51786/messier-50/>

Rieke, G. H., and Cambridge University Press, 2012. *Measuring the universe : a multiwavelength perspective*, New York: Cambridge University Press.

Salpeter, E. 1955. 'The luminosity function and stellar evolution', *Astrophysical Journal*, 121, pp. 161-167.

Villaume, A., Brodie, J., Conroy, C., Romanowsky, A. J. and Dokkum, P. 2017. 'Initial Mass Function Variability (or Not) among Low-velocity Dispersion, Compact Stellar Systems'. *The Astrophysical Journal*, 850(1), pp. 1-6.

Williams, D. R. 2018. 'Sun Fact Sheet', *NSSDCA*, viewed 23 May 2022. <https://nssdc.gsfc.nasa.gov/planetary/factsheet/sunfact.html>